nature communications

Article

https://doi.org/10.1038/s41467-025-63640-7

Constructing artificial neurons with functional parameters comprehensively matching biological values

Received: 8 October 2024

Accepted: 22 August 2025

Published online: 29 September 2025

Check for updates

Shuai Fu[1], Hongyan Gao[1], Siqi Wang[1], Xiaoyu Wang[1], Trevor Woodard[2], Zhien Wang[3], Jing Kong[3], Derek R. Lovley[2,4] & Jun Yao[1,4,5]

The efficient signal processing in biosystems is largely attributed to the powerful constituent unit of a neuron, which encodes and decodes spatiotemporal information using spiking action potentials of ultralow amplitude and energy. Constructing devices that can emulate neuronal functions is thus considered a promising step toward advancing neuromorphic electronics and enhancing signal flow in bioelectronic interfaces. However, existent artificial neurons often have functional parameters that are distinctly mismatched with their biological counterparts, including signal amplitude and energy levels that are typically an order of magnitude larger. Here, we demonstrate artificial neurons that not only closely emulate biological neurons in functions but also match their parameters in key aspects such as signal amplitude, spiking energy, temporal features, and frequency response. Moreover, these artificial neurons can be modulated by extracellular chemical species in a manner consistent with neuromodulation in biological neurons. We further show that an artificial neuron can connect to a biological cell to process cellular signals in real-time and interpret cell states. These results advance the potential for constructing bio-emulated electronics to improve bioelectronic interface and neuromorphic integration.

The boundary between electronics and biosystems is an increasingly important research area[1]. On one hand, biosystems provide enormous inspiration for advancing electronics through functional emulations[2–4]; on the other hand, bio-emulated electronics are often used to interface with biosystems to gain further biological understanding or improve biological functions[5–7]. These two directions often benefit each other mutually. A notable example is the development of memristors and associated neuromorphic electronics. The analog conductance modulation in nonvolatile memristors was initially used to emulate synaptic plasticity[8], which was later incorporated into neural computing networks[9–11]. Similarly, the spontaneous conductance relaxation in some volatile memristors has been employed for constructing basic integrate-and-fire neuronal functions[12,13], with potential applications for spiking neural networks. Concurrently, the bio-emulated functions of these neuromorphic devices make them promising candidates for improving signal translation in bioelectronic interfaces[14–19].

Developing artificial neurons with improved functionalities is of particular interest because neurons inherently possess rich computing capabilities[12,13]. Expanding the functionality of artificial neurons to more closely match their biological counterparts can lead to more efficient signal processing with reduced circuitry and energy consumption[13,14], which is especially beneficial for bioelectronic interfaces. To achieve this, artificial neurons have been constructed using various devices to emulate basic neuronal functions, such as spiking

[1]Department of Electrical and Computer Engineering, University of Massachusetts, Amherst, MA, USA. [2]Department of Microbiology, University of Massachusetts, Amherst, MA, USA. [3]Department of Electrical Engineering and Computer Science, Massachusetts Institute of Technology, Cambridge, MA, USA. [4]Institute for Applied Life Sciences, University of Massachusetts, Amherst, MA, USA. [5]Department of Biomedical Engineering, University of Massachusetts, Amherst, MA, USA. e-mail: juny@umass.edu

generation and signal integration[12–14,18,20–35]. The integration functions are further utilized to process bioelectronic signals from environmental, bodily, and physiological stimuli for bio-realistic interpretation[14–18,31–35].

Despite advancements in functional emulation, a significant gap remains between artificial neurons and their biological counterparts. Specifically, biological neurons use ultralow signal amplitudes (e.g., action potentials of 70–130 mV)[36], whereas demonstrated artificial neurons work with amplitudes ≥0.5 V[12,18,20–35]. The ultralow amplitudes facilitate seamless signal flow between sensory and computing functions in biosystems, enabling exceptional processing efficiency. Therefore, achieving parameter matching is crucial for enhancing efficiency in bio-emulated/integrated systems, including improving signal translation in bioelectronic interfaces. Recently, memristors with ultralow operating voltages were used to create artificial neuronal components, demonstrating that bio-amplitude signals (e.g., <130 mV) could induce state changes[16,25,32,37]. The state change was further manifested by threshold event of a current spike mimicking neuronal firing[32]. However, the discontinued (one-time) current spike still differs from repeated voltage spikes seen in actual neuronal firing, limiting the potential for signal cascading and realistic bioelectronic interactions.

We demonstrate artificial neurons capable of integrating bio-amplitude signals and producing continuous voltage spikes that resemble action potentials. The artificial neurons are built from a type of memristor uniquely designed to operate with ultralow voltage and current signals. The construct incorporates components that can fundamentally emulate key dynamic processes involved in neuronal firing. As a result, these artificial neurons achieve not only close functional emulation but also parameter matching in crucial aspects such as signal amplitude, spiking energy, temporal features, frequency response, and dynamics tuning. Moreover, these artificial neurons can be integrated with chemical sensors to emulate neuromodulation by extracellular substances (e.g., ions and neurotransmitters) in a manner consistent with biological neurons. Furthermore, we demonstrate that an artificial neuron can connect to a biological cell to process cellular signals in real time and interpret cell states. These advancements enhance the potential for constructing bio-emulated electronics to improve bioelectronic interface and neuromorphic integration.

Results

The constituent bio-amplitude memristor

A biological neuron can be stimulated by injected excitatory postsynaptic currents (EPSCs) to raise its intracellular charge (Q), thus the membrane potential (Fig. 1a, top panel). The charge accumulation (ΔQ) is the competing result of EPSC injection (I) and membrane current leakage (I'), or $\frac{\Delta Q}{\Delta t} = I - I'$. Upon a certain threshold, it triggers the broad opening of sodium channels for Na^+ influx to quickly raise the membrane potential, forming the fast depolarization in an action potential[36]. Coincidently, the atomic accumulation (ΔN) of the filament in a memristor can be similarly viewed as the competing result of the ionic current injection (I_{M+}) and leaky current (I'_{M+}) diffusing outward the filamentary volume (Fig. 1a, bottom panel), or $\frac{\Delta N}{\Delta t} = I_{M^+} - I'_{M^+}$. As a result, the atomic integration process in a memristor can mimic the charge integration in a neuron[25]. The eventual filament bridging is like triggered depolarization. At the peak of depolarization, the sodium channels are self-deactivated for entering into the repolarization phase[36]. Although self-deactivation is absent in a memristor, the instability of filament in some volatile memristors can be utilized for facilitation[21]. These inherent dynamics of filamentary volatile memristors make them promising candidates for emulating the integration function of biological neurons[12,13].

However, biological neurons achieve the integrate-and-fire function with very low amplitudes in key parameters, including ultralow action potential amplitudes (e.g., <130 mV) that serve as the fundamental processing signal. The efficient charge selectivity across the cell membrane also ensures that an injected current as low as several nanoamperes (nA) can generate sufficient potential to elicit an action potential[36]. These parameters result in ultralow spiking energy (e.g., 0.3–100 pJ)[38–40], which ensures biocomputational efficiency and maintains a safe, non-reactive electrochemical environment. To achieve parameter matching in an artificial neuron, one conceivable approach is to use a memristor with functional parameters (e.g., voltage, current) that fall within biological ranges. Nevertheless, most filamentary memristors operate at voltages >0.5 V. Among the few that achieved bio-amplitude voltages, the reported working currents were typically >1 μA[14,41].

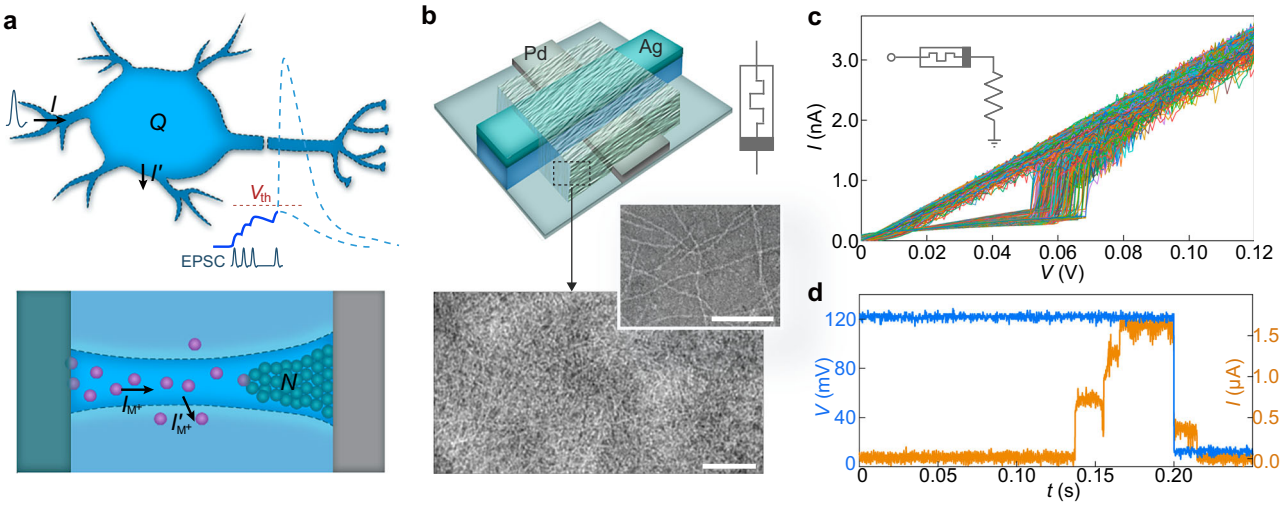

Fig. 1 | Constructing memristor working with biological parameters. a (Top) Schematic of an integrate-and-fire neuron model involving EPSC injection (I) and membrane current leakage (I'). The blue curve illustrates the evolution of membrane potential by charge integration from competing I and I'. Depending on whether the integration reaches the threshold (V_{th}) or not, it can either elicit an action potential or fade away (dashed lines). (Bottom) Schematic of the dynamics of a metal filament formation in a memristor. The dashed lines delineate the filamentary volume. The purple dots indicate metal ions (M^+). **b** (Top) Schematic of the memristor structure involving protein nanowires. (Bottom) Transmission electron microscope (TEM) images of protein nanowires in a sparse (upper) and dense (lower) network. Scale bars, 100 nm. **c** 1000 I-V sweeps from a fabricated memristor connected with a resistor (inset). **d** Current (orange) response in a memristor applied with a voltage pulse (blue). The amplitude of the pulse switched from 120 mV to 10 mV (as reading voltage) at $t = 0.2$ s.

We previously demonstrated that thin films assembled from protein nanowires harvested from the microbe Geobacter sulfurreducens can be used in device applications due to their excellent stability[25,42–44], which is attributed to their design as extracellular structures in natural environments. Their molecular size (e.g., 2–3 nm diameter) ensures that the assembled thin film has a dense structure similar to that of a conventional dielectric (Fig. 1b, bottom). Specifically, they are designed to facilitate the microbe's charge exchange involved in redox processes[42]. Introducing the protein nanowires into an Ag-based memristor significantly reduced the functional voltage to bio-amplitude regime[25], although the switching performance under ultralow current has not yet been studied. Therefore, we constructed memristors with a similar device structure (top, Fig. 1b; Supplementary Fig. 1) to study switching behavior with current injections at biological levels (e.g., 2 nA). To restrict the current, a series resistor (28 MΩ) was connected to the memristor. A continuous series of 1000 voltage sweeps (0→120 mV→0) were applied to the device (Fig. 1c). The recorded *I-V* curves reveal several key features desirable for constructing artificial neurons. First, the memristor consistently switched to On states at voltages of ~60 mV and current levels of ~1.7 nA. Both values fall within biological ranges[36], supporting the feasibility of constructing artificial neurons with parameters that match biological ones. The Off states maintained a resistance ~200 MΩ, close to the high membrane resistance in cells (e.g., 50–300 MΩ)[45]. Second, the *I-V* curves consistently started with an Off state during the consecutive sweeps, showing characteristic volatile switching. The volatility can facilitate the emulation of sodium-channel closure during repolarization. Third, the continuous sweeps yielded narrow distributions of switching voltages (e.g., 60 ± 3 mV S.D.) and currents (e.g., 1.76 ± 0.06 nA S.D.), demonstrating a stability not achieved in other bio-amplitude memristors[14]. Statistics across different devices showed consistent narrow distributions of these parameters (Supplementary Fig. 2). The switching stability is also crucial for constructing artificial neurons with consistent firing characteristics.

We further examined the switching dynamics of the memristor using pulsed signals (Fig. 1d). Note that the current compliance was lifted due to reduced current resolution in pulsed measurements. When a 120-mV input was applied, the memristor exhibited an integration period before transitioning to the On state (t ~ 0.13 s). As discussed before, this integration period reflects the atomic accumulation in the forming filament, which can emulate the charge integration process in a neuron (Fig. 1a). After the pulse ended (t ~ 0.2 s; followed by a 10-mV reading pulse), the memristor exhibited a delay before transitioning to the Off state (t ~ 0.21 s), indicating a spontaneous filament rupture. This filament rupture requires the cessation of external input, which does not fully replicate the self-regulated closure of the sodium channels during repolarization[36]. Consequently, previously constructed artificial neurons by directly employing the switching dynamics could not relax to a rest state for continuous firing[21,25,32].

Bio-amplitude artificial neuron

To fully utilize the memristor's multiple bio-amplitude functional parameters and overcome previous limitations, we constructed an artificial neuron by integrating the memristor with an RC circuit (Fig. 2a). Voltage pulses (120 mV, 5 ms) at physiologically relevant frequencies (10–100 Hz)[46] were used as emulated action potential input. Unlike previous artificial neurons that could only produce a current output[21,25,32], our design employs the voltage across the capacitor as output (V_o), enabling a voltage-to-voltage signal translation similar to that in biological neurons.

We analyzed the functional dynamics of the artificial neuron as follows. Initially, with the memristor's high Off resistance (~200 MΩ), the input voltage primarily drops across the memristor. This leads to the atomic accumulation in the filament, which emulates the charge integration in a neuron (Fig. 2b-i). Once the filament forms (i.e., the memristor turns On), it causes rapid charging of the capacitor, emulating the broad opening of sodium channels for fast depolarization[36] (Fig. 2b-ii). As the capacitor's value (33 nF) is close to that of cell membranes[47] and the memristor's current density (~250 nA/nF) is similar to the collective sodium channels[48], the capacitor charges at a rapid rate (e.g., > 250 V/s) akin to that during fast depolarization in cells[36]. Importantly, the charged capacitor then imposes a reverse bias to the memristor, promptly resetting it to Off. This mimics the self-regulated closure of the sodium channels (inactivated by the elevated membrane potential) at the end of depolarization, which was absent in previous constructs[21,25,32]. Subsequently, the charged capacitor discharges through the resistor (R) to reduce V_o, emulating the membrane discharge through potassium channels during repolarization[36] (Fig. 2-iii). The R value (~1 MΩ) used is within the range of equivalent resistances of collective potassium channels[49,50]. Notably, the elevated V_o during this repolarization depresses the voltage drop across the memristor from continuous pulsed inputs. Our investigations revealed that an internal relaxation (when V_i = 120 mV) and external facilitation (when V_i = 0 V) combine to reset the memristor during repolarization (Supplementary Fig. 3), effectively creating a refractory period that prevents firing before the completion of repolarization—mirroring the behavior of biological neurons.

The above analysis was supported by experimental results shown in a representative neuronal firing (Fig. 2c, d). The spiking output exhibited an amplitude up to ~120 mV, matching the input. Each spike rapidly reached its peak and then declined without plateauing, which is attributed to the self-regulation mechanism discussed earlier. The incorporation of an effective refractory period allowed the spiking amplitude to return to a baseline close to 0 V to complete the full cycle (Fig. 2d). As a result, the spiking output can also serve as input to a downstream artificial neuron to elicit firing (Supplementary Fig. 4), demonstrating the potential for constructing cascading spiking logic or networks. Spiking width of 1–5 ms that is close to those in biological neurons can be achieved by adjusting the RC constant of the circuit (Supplementary Fig. 5). Stochastic variations in both firing frequency and amplitude were observed, due to the inherent stochastic dynamics of the memristor[51]. Specifically, stochastic fluctuations in the filament formation can lead to variable signal integration (thus firing frequency), while variations in On conductance influence the charging rate (thus the amplitude). A decrease in the variability with the increasing firing frequency was observed (Supplementary Fig. 6), consistent with observations in biological cells[52]. Stochastic neuronal activity is crucial for enhancing information processing related to complex behaviors and cognitive functions. Consequently, artificial neuronal components with inherent stochasticity are considered promising candidates for developing stochastic computing systems[51].

We further investigated the frequency response in the artificial neuron. In biological neurons, the charge loss through membrane leakage is proportional to the time interval between neighboring EPSC spikes (Fig. 1a, top). Consequently, reducing the interval (e.g., increasing the input frequency) decreases the leakage loss and improves the stimulation efficiency (e.g., output-to-input ratio)[53,54]. This improvement eventually levels off due to reaching a maximum[55]. This nonlinear input-output relationship enriches spatiotemporal information encoding. The artificial neuron exhibited a similar output trend (Fig. 2e), in which the stimulation efficiency gradually increased, then decreased (e.g., ~33 Hz), and eventually reached saturation (e.g., >60 Hz). The trend was consistently observed with varied input spikes and frequency ranges (Supplementary Fig. 7). The artificial neuron replicates the above neuronal behaviors because: 1) the atomic accumulation in the memristor's filament, which underlies input integration, involves competing injection and leakage processes similar to those in neuronal charge integration (Fig. 1a), and 2) the reverse bias by the charged capacitor creates a comparable 'refractory' period (Fig. 2b-

https://doi.org/10.1038/s41467-025-63640-7

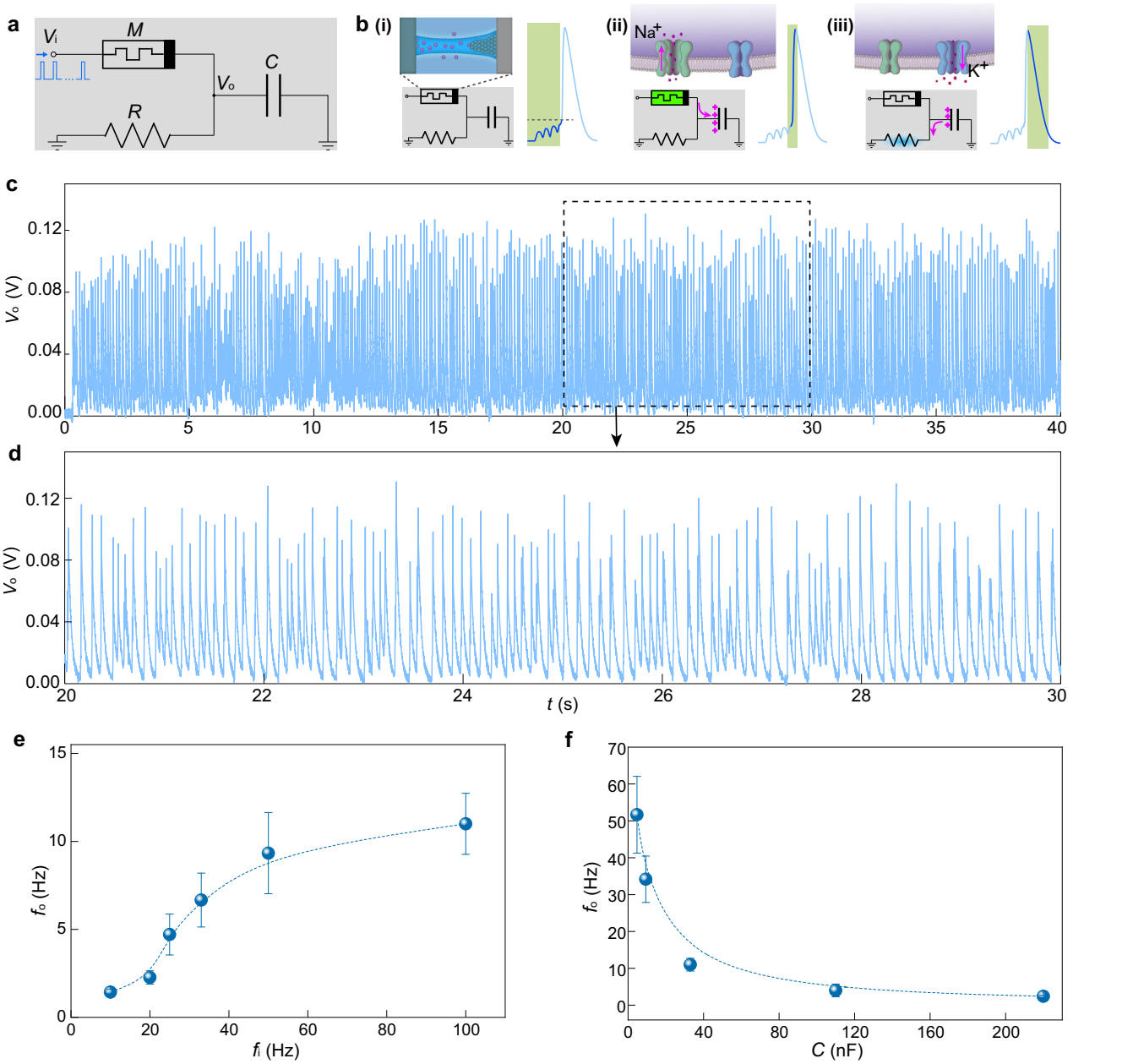

Fig. 2 | Constructed artificial neurons and performance. a Circuit diagram of the artificial neuron. **b** Different stages in neuronal output. (i) The artificial neuron undergoes atomic integration in the filament of the memristor, emulating the (subthreshold) charge integration for eliciting an action potential. (ii) The turned-on memristor leads to rapid charging to the capacitor, emulating the broad opening of Na^+ channels for fast depolarization. (iii) The charged capacitor imposes a reverse bias on the memristor to turn it off and discharges through the resistor, emulating the self-regulated closure of Na^+ channels and opening of K^+ channels for repolarization. **c** A representative output from a constructed artificial neuron. The input was a series of pulses (120 mV, 5 ms) with a frequency of 100 Hz. **d** Zoom-in firing features from the dashed box in (**c**). **e** The output firing frequency (f_o) in an artificial neuron with respect to the input frequency (f_i). **f** The firing frequency with respect to the capacitor value used. The input frequency was fixed at 100 Hz. Data in (**e**) and (**f**) are presented as mean values ± SD (error bar).

iii) that leads to output saturation. The temporal dynamics also enabled the artificial neuron to respond differently to key neuronal firing patterns such as tonic, burst, and adapting activities (supplementary Fig. 8), suggesting the potential for constructing computational networks.

The firing dynamics in the artificial neuron can be adjusted based on its mechanistic similarity to biological neurons. Existing studies indicate that modulating membrane capacitance in neurons affects firing frequency, with a lower capacitance leading to an increased firing rate[56]. This can be generally understood by the leaky-capacitor model, where a lower capacitance results in a smaller time constant. A similar trend was observed in the artificial neuron, where decreasing capacitance C led to an increase in output frequency (Fig. 2f). Notably, with a value ($C = 4.7$ nF) typical of cell membrane capacitance, the artificial neuron achieved a spiking energy of ~37 pJ. Further reducing the capacitance to 0.5 nF or 50 pF resulted in an estimated spiking energy of ~3.5 pJ or 0.2 pJ (Supplementary Figs. 9, 10). These values are comparable to those in biological neurons (e.g., 0.3–100 pJ)[38–40]. While previous transistor or CMOS-based artificial neurons achieved similar or even lower spiking energy[57–59], our design represents the first one with both voltage and energy amplitudes strictly confined within the biological ranges (Supplementary Table 1)[18,20–24,26–35,57–60]. As a result,

the constructed artificial neuron can directly process emulated real neuronal signals captured by patch clamp and output spiking signals having key parameters (e.g., current, voltage, frequency) matching neuronal action potentials (Supplementary Fig. 10). Similarly, as R emulates potassium channels, decreasing its value resulted in faster repolarization and a corresponding increase in output frequency (Supplementary Fig. 11). It is noteworthy that these bio-realistic energy and frequency trends were achieved with bio-amplitude input/output, representing a significant advancement in bio-emulation beyond previous achievements.

Chemical neuromodulation

Neuromodulation by the extracellular chemical environment enriches information flow and neural connectivity to improve biocomputation[61]. Therefore, developing chemically modulable artificial neurons is highly relevant for neuromorphic computing and biointegration. Many chemical stimuli influence ion channels to realize neuromodulation[62] (Fig. 3a). Our analysis indicates that the R in the artificial neuron mimics the role of potassium channels (Fig. 2b-iii). Thus, translating chemical sensing into modulation of R could enable emulated neuromodulation in the artificial neuron.

To this end, the resistor R was replaced by an n-type transistor T_O, with its gate connected to a voltage divider consisting of a resistor R_1 and a chemiresistor S (Fig. 3b, c). The resistance change in S translates into a gate voltage change (ΔV) that modulates the transistor's conduction. The transistor also amplifies the signal change. It has a threshold ~0.14 V (Supplementary Fig. 12a), so a bio-amplitude ΔV (0–120 mV) remains in the subthreshold region and can induce significant resistance changes in the transistor. The resulting modulable resistance range of 0.2–1.3 MΩ (Supplementary Fig. 12b) is consistent with the estimated equivalent resistance of potassium channels. Consequently, this chemically modulable artificial neuron continues to operate with bio-amplitude signals.

We demonstrated neuromodulation with different chemical species. Sodium ions, prevalent in the extracellular environment, modulate cell excitability[63]. An increase in extracellular sodium concentration has been shown to increase the firing rate, presumably because higher concentrations accelerate sodium-channel recovery from inactivation[64]. We fabricated a PEDOT:PSS chemiresistor for sodium sensing[65] (Supplementary Fig. 13). The chemiresistor exhibited a consistent resistance increase with rising sodium concentration in the physiological range of 0–150 mM (Fig. 3d, dashed line). The result is consistent with the de-doping effect caused by diffusing sodium ions in PEDOT: PSS[65]. The resistance increase raised the gate voltage applied to T_O, thereby enhancing its conductance and promoting faster repolarization. The firing frequency of the artificial neuron increased monolithically with sodium concentration (Fig. 3e), consistent with both our analysis and trends observed in biological experiments[66]. The saturation trend (e.g., >50 mM) was attributed to sensing saturation at high concentrations (Fig. 3d).

Neurotransmitters are another key category of substances involved in neuromodulation. Dopamine, a prominent example, can bind to various types of receptors, leading to both excitatory and inhibitory effects depending on its concentration[67]. At low concentrations, its predominant effect by binding to D2 receptors enhances cell excitability. In contrast, at high concentrations, its predominant effect by binding to D1 receptors can suppress cell excitability. Consequently, dopaminergic modulation exhibits an ambipolar profile with respect to concentration, highlighting dopamine's diverse roles in neuromodulation[68].

We constructed a graphene chemiresistor with an ambipolar sensing profile to emulate dopaminergic modulation (Supplementary Fig. 14). The sensor channel was immersed in dopamine solution, and a gate voltage was applied through a carbon electrode placed in the solution (Fig. 3c). Note that part of the applied voltage V_g drops across the electric double layer at the carbon electrode (Fig. 3f, inset). Dopamine oxidization at the interface generates faradic conduction, which reduces the interfacial voltage drop and increases the effective gate voltage (V_{eff}) applied to the graphene channel (red arrows)[69]. As dopamine concentration increases, V_{eff} applied to the graphene channel also increases, shifting graphene's transport curve in the negative direction (Fig. 3f). For a given V_g, this shift can cause the transport to cross the Dirac point, resulting in an ambipolar profile (dashed line). Consequently, the graphene sensor exhibited an ambipolar resistance change in response to dopamine concentrations within the physiological range (e.g., 0–256 μM). This ambipolar resistance change was translated into an ambipolar conductance change in transistor T_O, producing an ambipolar firing trend consistent with that observed in biological neurons[68] (Fig. 3g). The modulation range (e.g., 25–34%) was close to the average range observed in biological neurons (e.g., 20–39%)[70]. As dopamine plays a critical rewarding role, this ambipolar modulation can help to balance exploiting known rewards and new possibilities for enhancing cognitive learning[71].

The demonstrations above highlight the versatility in designing chemically modulable artificial neurons for bio-emulations. Neuromodulation by other chemical substances can be achieved using similar design principles. Importantly, these sensing components can be integrated in parallel to emulate the coexistence of multiple chemically regulated ion channels[62] (Supplementary Fig. 15a), provided that selective sensing is achievable. As a preliminary demonstration of this feasibility, we showed that selective sensing of sodium and dopamine is possible within physiologically relevant ranges (Supplementary Fig. 16). By employing strategies such as surface functionalization[72], molecular imprinting[73], and genetic engineering[74,75], broader sensing selectivity may be realized to enable the emulation of parallel and collective chemical signaling as observed in biological cells.

The neuromodulation described above employed a sensing circuit comprising a transistor T_O, a resistor R_1, and a chemiresistor S, which introduced additional energy consumption and integration complexity. For improvement, we developed a simplified design by replacing the entire sensing circuit with a standalone chemiresistor (Fig. 3h). The chemiresistor was made from a thin layer of poly(-benzimidazobenzophenanthroline) (BBL)[76], which exhibits conductance modulation in response to analytes via electrochemical interaction. Due to BBL's bipolar transfer characteristics[77], it enabled resistance tuning similar to that achieved with the original sensing circuit in response to dopamine and sodium (Fig. 3i). As a result, the artificial neuron retained comparable firing modulation trends (Fig. 3j). Importantly, this simplified chemical neuron can maintain the same spiking energy as the original neuron, because energy consumption is primarily determined by capacitor charging and is largely unaffected by S (Supplementary Fig. 17). The overall energy consumption is reduced by at least two orders of magnitude compared to previously reported chemical artificial neurons (Supplementary Table 1)[18,24,26,60]. For this simplified design, the entire neuronal circuit can be fabricated on a silicon substrate using standard CMOS-compatible fabrication processes (Supplementary Fig. 18). The design can also lead to a simplified version of artificial neuron integrated with parallel sensors to emulate the coexistence of multiple chemically regulated ion channels (Supplementary Fig. 15b).

Connecting to biological cells

One of the main visions in bioelectronics is to blur the boundary between electronics and biosystems, enabling seamless integration for 'cyborg' systems[1,78]. In addition to enhancing material and structural compatibility[78,79], improving interfacial signal translation is another crucial aspect[17]. Artificial neurons have the potential to facilitate efficient interfacial signal translation and enable cell-resolution information flow. While previous studies have explored the use of artificial

https://doi.org/10.1038/s41467-025-63640-7

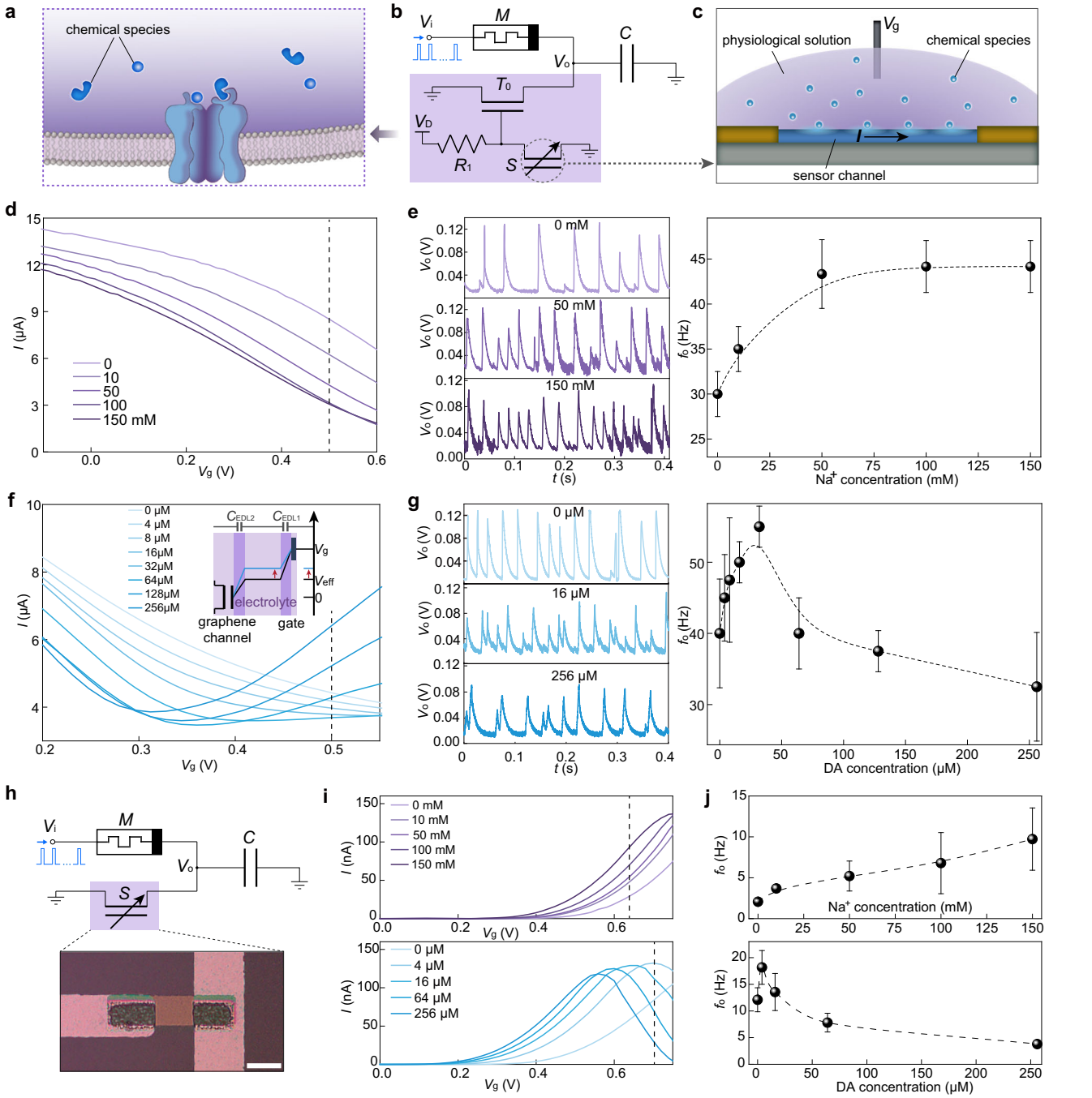

Fig. 3 | Chemically modulable artificial neurons emulating neuromodulation. **a** Schematic of neuromodulation by chemical species binding to an ion channel. **b** Circuit diagram of the chemically modulable artificial neuron (V_D = 0.12 V). The chemiresistor (S) modulates the transistor (T_o) that is responsible for capacitor discharge (purple region), which is analogous to the chemical modulation of ion channels. **c** General structure of a chemiresistor and sensing setup. **d** Transport curves of a PEDOT:PSS chemiresistor immersed in solutions of different Na^+ concentrations. A constant bias (V_{ds}) of 10 mV was applied across the two terminal electrodes during the gate (V_g) sweeps. A fixed gate voltage of 0.5 V was applied to the chemiresistor in the artificial neuron (dashed line), and a R_1 = 3 kΩ was used. **e** (Left) Representative outputs from the artificial neuron exposed to different Na^+ concentrations. (Right) Summarized trend of the firing frequency (f_o) with respect to Na^+ concentration. **f** Transport curves of a graphene chemiresistor immersed in solutions of different dopamine (DA) concentrations. A constant bias of 10 mV was applied across the two terminal contacts during the gate sweeps. A fixed gate voltage of 0.5 V was applied to the graphene sensor in the artificial neuron (dashed line), and a R_1 = 1.5 kΩ was used. The inset shows the voltage distribution in the sensing system. The applied V_g is distributed across two capacitive layers (electric double layers (EDLs)) at the gate electrode (C_{EDL1}) and the graphene channel (C_{EDL2}). **g** (Left) Representative outputs from the artificial neuron exposed to different DA concentrations. (Right) Summarized trend of the firing frequency with respect to DA concentration. **h** Simplified design of the chemically modulable artificial neuron. The bottom shows an optical image of the BBL chemiresistor. Scale bar, 20 μm. **i** Transport curves (V_{ds} = 100 mV) of the BBL chemiresistor responding to different (top) Na^+ and (bottom) DA concentrations, with a constant gate voltage of 0.64 V and 0.7 V applied, respectively (dashed lines). **j** Summarized trends of the f_o with respect to (top) Na^+ and (bottom) DA concentrations, respectively. Data in the right panels of (**e**) and (**g**), and (**j**) are presented as mean values ± SD (error bar).

https://doi.org/10.1038/s41467-025-63640-7

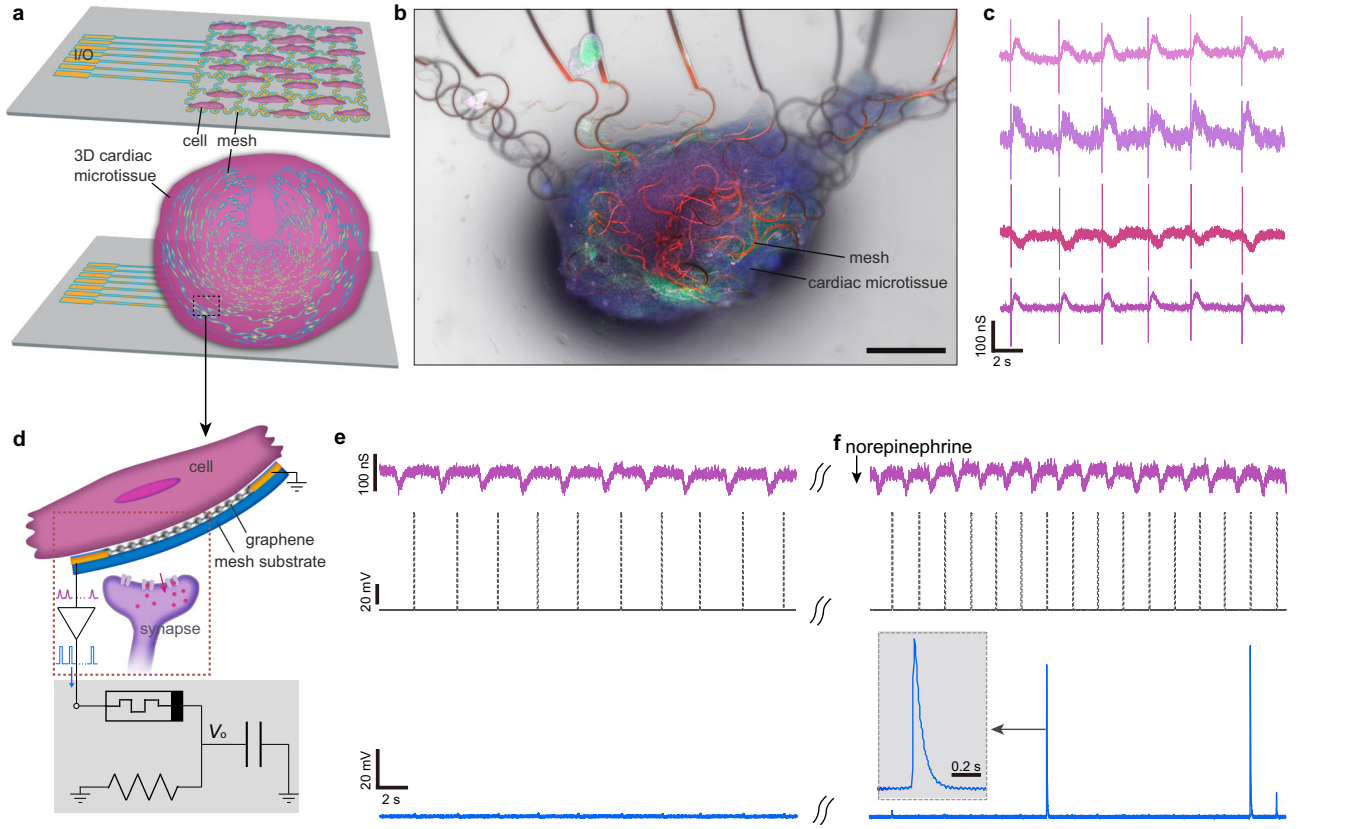

Fig. 4 | Connecting the artificial neuron to a biological cell. a (Top) Schematic of seeding cardiac cells (cardiomyocytes) on an ultra-flexible and releasable mesh sensing system. (Bottom) Schematic of forming 3D mesh-tissue integration. **b** Fluorescence optical image of a formed mesh-tissue. The red color indicates the embedded mesh ribbons. The green, blue, and purple colors indicate F-actin, 4′,6-diamidino-2-phenylindole (DAPI), and cardiac Troponin T (cTnT) in the cells, respectively. Scale bar, 0.5 mm. **c** Representative recordings from four graphene sensors integrated on a mesh embedded in a tissue. The sharp spikes and broad peaks correspond to electrical action potentials and mechanical contractile signals, respectively. **d** Schematic of the cell-sensor interface in the mesh-tissue system. The acquired sensing signals are amplified and fed into the artificial neuron, analogous to that presynaptic signals are transmitted by a synapse to the postsynaptic neuron. **e** Sensing signals (f ~ 0.4 Hz) recorded from a cell in a mesh-embedded tissue (top panel) were converted into voltage pulses (120 mV, 70 ms, middle panel) and fed into the artificial neuron, which remained silent (bottom panel). **f** Sensing signals of increased frequency (f ~ 0.6 Hz) from the cell after the tissue was treated with norepinephrine (top panel) were converted into voltage pulses (120 mV, 70 ms, middle panel) and fed into the artificial neuron, which showed firing activities (bottom panel).

neuronal components for processing environmental signals or post-recorded cellular signals, real-time cellular signal processing has not been demonstrated[14–18,31–35]. We aimed to showcase the feasibility of 'cell'-to-cell signal translation. For this purpose, we used cardiomyocytes, which exhibit electroactivity (e.g., action potentials) similar to neurons—for the following reasons: 1) cardiomyocytes develop spontaneous electroactivity more rapidly than neurons, and 2) their electroactivity is more robust (e.g., periodic firing) and physiologically interpretable (e.g., contractile function).

To capture cellular electroactivity, we constructed a bioelectronic mesh sensing system to interface with cardiac tissue (Fig. 4a; Supplementary Fig. 19). The mesh was fabricated following a previously established procedure (Supplementary Fig. 20)[79]. Briefly, an ultrathin polymeric mesh scaffold (~0.5-μm thick SU-8) was lithographically defined on a releasable layer (150 nm Ge). An array of graphene sensors was patterned and addressed by interconnects (100 nm Au), which were further passivated (80 nm Si_3N_4) to prevent leakage in physiological solutions. The completed mesh system was released from the substrate and seeded with human embryonic stem cell-derived cardiomyocytes (hESC-CMs). Note that individual ribbons in the mesh had a thickness of ~2 μm and a lateral size of ~20 μm (Supplementary Fig. 19), yielding an ultra-flexible mechanical property similar to that of tissue[5]. Consequently, the mesh was gradually folded and engulfed by the developing tissue to form 3D tissue embedment (Fig. 4b; Supplementary Fig. 21). The cellular action potentials can be detected by the embedded graphene sensors through the field effect, while cellular contractions can be detected through the piezoresistive effect[79,80]. As a result, the graphene sensors, with a size (e.g., $20 \times 20\ \mu m^2$) smaller than a cell (Supplementary Fig. 19), effectively captured the electroactivity of coupled action potentials and contraction from individual cells (Fig. 4c).

The cell-sensor junction can be conceptualized as an emulated synaptic junction, with the physiological signals captured representing pre-synaptic inputs. We incorporated a circuit component to amplify the acquired signals into bio-amplitude pulses, which encode the firing frequency of the cardiomyocyte (Fig. 4d; Supplementary Fig. 22). We emphasize that the inclusion of the amplifying component is not fundamentally required for interfacing, as demonstrated by our artificial neuron's inherent ability to directly process real neuronal signals (Supplementary Fig. 10). This added component serves as a workaround for limitations in current sensing technology, rather than any intrinsic constraint of neuronal function. Conventional extracellular sensors are passive and lack the synapse-like excitability needed to fully capture and restore action potential signals[81]. If future advancements achieve near-complete amplitude capture, this additional element could be removed entirely. Even in this workaround form, our demonstration retains the merit, as it represents a standalone bio-interface operating without the use of programmable microcontrollers

or computer-based systems typically used for bio-signal preprocessing[82,83], underscoring its potential to reduce integration complexity.

Unlike other electroactive cells (e.g., the physiological relevance of individual neuronal firing only signifies in the context of grouped activities[5]), the spiking frequency in a cardiomyocyte is directly linked to cardiac contractile function. This direct relationship facilitates a straightforward interpretation of the output in the artificial neuron. In our study, we used the artificial neuron to differentiate between normal and drugged cell states. Specifically, cultured cardiac tissue exhibited a typical firing frequency of ~0.4 Hz, as indicated by the recording signals (Fig. 4e, top). This frequency corresponded to a spiking interval >2.5 s in the converted inputs (middle). The prolonged interval led to substantial atomic leakage and hindered filament formation in the memristor as previously discussed. Consequently, the artificial neuron remained silent (bottom).

We then treated the cardiac tissue with norepinephrine, a β-Adrenergic receptor agonist used in heart failure treatment. Perfusing the cardiac system with norepinephrine (10 μM) resulted in an increased firing frequency[80], which was clearly captured by the recording signals (Fig. 4f, top). The frequency increased to ~0.6 Hz, reducing the spiking interval to ~1.7 s in the converted inputs (middle). This change in input frequency shifted the filament dynamics to net accumulation in the memristor. As a result, the artificial neuron was stimulated to fire (bottom), suggesting the changed state in the biological cell. Clinical diseased state of arrhythmia features irregular bursts of high-frequency beating. Although the feature is challenging to reproduce in in vitro tissue, the artificial neuron successfully captured the arrhythmic phases when fed with emulated inputs converted from clinical recordings (Supplementary Fig. 23). These results suggest that artificial neurons can feasibly interpret biological cellular signals in real-time.

Discussion

We have constructed artificial neurons that achieve close bio-emulations by leveraging the unique dynamics of a memristor fabricated from a bio-derived electronic material. The constructed artificial neurons are highlighted not only by the functional similarity to biological counterparts but also by parameter matching in key metrics of signal amplitude, frequency, energy, and output trend, transcending previous constructs that focused solely on functionality. The analysis of the artificial neuron's performance reveals mechanisms closely resembling biological dynamics, providing a convenient platform for biomimetic modulation. Its functionality is readily expanded by integrating chemical sensors, enabling chemically modulable behaviors akin to neuromodulation. These properties point to the unique potential of the artificial neuron for developing neuromorphic systems with improved energy efficiency and environmental adaptivity. The demonstrated 'cell'-to-cell signal flow between the artificial neuron and a biological cell, despite being in a preliminary form, can spearhead the feasibility of creating more effective bioelectronic interfaces. The work suggests a promising direction toward developing bio-emulated electronics, which in turn can lead to closer interface with biosystems.

Methods

Fabrication of memristors

The bottom electrode (Cr/Pd = 3/25-nm thick, 20-μm wide) was defined by standard photolithography, metal evaporation, and lift-off process on a Si wafer capped with 600 nm thermal SiO_2 (Nova Electronic Materials). A layer of HfO_2 (5 nm) was then deposited by atomic layer deposition (ALD). The top electrode (Cr/Ag/Pd = 5/50/20-nm thick, 20-μm wide) was defined by standard photolithography, metal evaporation, and lift-off process. Reactive ion etching (RIE, 2-sccm O_2 + 16-sccm CHF_3, 150 W for 5 min) was used to etch away the HfO_2 layer outside the electrode region and expose the vertical edge. The HfO_2 layer serves as a spacer to define an accurate spacing between the top and bottom electrodes for drop-casted protein nanowires. This vertical structure is topologically equivalent to a planar nanogap device structure (Supplementary Fig. 24). Alternatively, the HfO_2 layer was replaced by a SiO_2 layer (28 nm) deposited by evaporation. The protein nanowires were harvested, purified from *G. sulfurreducens*, and suspended in water solution as previously described[25,43]. The solution (~25 μL/cm^2) was drop-casted on the device area (20 × 20 μm^2) and dried at 80 °C for 3 min to complete the device structure. The nanowire networks were imaged by using a transmission electron microscope (TEM, JEM2200FS; JEOL).

Fabrication of PEDOT:PSS chemiresistors

The bottom electrode (5/50 nm, Cr/Au) was defined by standard photolithography, metal deposition, and lift-off process on a glass wafer. PEDOT:PSS solution (1.3 w% in H_2O; Sigma-Aldrich) was then spin-coated on the substrate (1600 rpm for 30 s) and baked at 140 °C for 10 min to yield a thin-film thickness of 80 ~ 100 nm. The whole substrate was immersed in dimethylsulfoxide (DMSO, Thermo Fisher Scientific) for 30 min and annealed in air at 140 °C for 1 h. The PEDOT:PSS channel with a size of 100 × 300 μm^2 was defined by lithographically patterning a protective resist (AZ4620; AZ Electronic Materials), oxygen-plasma etching (180 W, 100-sccm O_2, 10 min) of unprotected PEDOT:PSS, and removal of the resist. 500-nm SU-8 (2000.5; Kayaku Advanced Materials) was spin-coated on the substrate, lithographically patterned, and hard baked to passivate/insulate the electrodes and interconnects.

Fabrication of graphene and BBL chemiresistors

Monolayer graphene synthesized on a copper foil[84] was spin-coated (1000 rpm, 1 min) a layer of PMMA 950 A4 (Kayaku Advanced Materials) baked at 80 °C for 3 min. Then the sample was floated on Cu etchant (CE-100; Transene, Inc.) for 30 min to remove the Cu foil. The released PMMA/graphene film was rinsed with deionized (DI) water 10 times and transferred onto a Si substrate capped with 600 nm thermal SiO_2. The substrate was baked (80 °C for 5 min + 130 °C for 30 min) to improve graphene adhesion. The PMMA film was removed by immersing the substrate in acetone for 30 min. Graphene channels (each ~25 × 15 μm^2) were defined by lithographically patterning a protective resist (LOR 3A + S1813; Kayaku Advanced Materials), oxygen-plasma etching (50 W, 20-sccm O_2, 30 s) of unprotected graphene, and removal of resist. The contacts and interconnects (5/50 nm, Cr/Pd) were defined by standard photolithography, metal deposition, and lift-off process. The contacts and interconnects were further passivated by sputtering a layer of Si_3N_4 (~100 nm) to prevent the current leakage in solution.

For the BBL chemiresistor, the bottom electrode (3/30 nm, Cr/Pt) was defined by standard photolithography, metal deposition, and lift-off process on a glass wafer. BBL solution was prepared by dissolving 15 mg BBL (Sigma-Aldric) into 3 ml Methanesulfonic acid (MEA) (Sigma-Aldric). The BBL solution was spin-coated on the substrate and immersed into DI water immediately for 12 hr. Then the substrate was baked at 80 °C for 10 min and annealed at 115 °C for 1 h. The BBL channel with a size of 25 × 15 μm^2 was defined by lithographically patterning a protective resist (LOR 3 A + S1813), oxygen-plasma etching (180 w, 40-sccm O_2, 10 min) of the unprotected BBL, and removal of the resist. The contacts and interconnects were lithographically passivated by a layer (~500 nm) of SU-8 (2000.5).

Fabrication of mesh sensing system

The mesh system was fabricated following a previous procedure (Supplementary Fig. 12)[79]. Briefly, a sacrificial layer (150-nm Ge) was deposited on a Si substrate capped with 600-nm thermal SiO_2. Then a 500-nm SU-8 layer (2000.5) was spin-coated on the substrate and hard

backed (for fluorescence imaging, 0.0008 wt% of Rhodamine 6G powder was mixed into the SU-8). Graphene was transferred onto the SU-8 substrate, lithographically defined with a protective resist layer (LOR 3A + S1813; Kayaku Advanced Materials), oxygen-plasma etched (50 W, 20-sccm O_2, 30 s) of the unprotected area to define a patterned array. A similar step was used to define a protective resist layer for defining the mesh pattern, etching the unprotected SU-8 film by RIE, and removing the protective resist layer. Standard photolithography and metal deposition were used to define the metal contacts and interconnects (Cr/Pd/Au/Pd, 3/15/40/5 nm), which were further passivated by a layer of Si_3N_4 (~80 nm). Finally, the fabricated mesh system was released from the substrate by etching the Ge layer in 1% H_2O_2 solution (30 min) and rinsed in DI water before cell culture.

Cell culture

Cardiomyocytes were differentiated from human embryonic stem cells hESCs (WAe009-A, H9) following our previously reported procedure[79]. Differentiated cells (at days 10–12) were transferred onto the mesh system for integration with the following procedures. The released mesh was sterilized (70% ethanol for 1 h), treated with Poly-D-lysine (0.1 mg/ml, Gibco) in incubator overnight, and embedded in 100 µL Matrigel (10 mg/ml). The resuspended cells were transferred onto the Matrigel with a density ($3–4 \times 10^6$ cells/cm^2) and incubated for 24 h. Then the cells were maintained using RPMI 1640 plus1% B27 by with the daily change of the medium. The electrical recordings typically started at day 5 of seeding (day 15–17 of differentiation).

Electrical measurements

The switching performance of the memristors, the transport and sensing performance of the PEDOT:PSS, BBL, and graphene chemiresistors were measured by a semiconductor analyzer (Keysight B1500A). The input signals to the artificial neurons were generated by a semiconductor analyzer (Keysight B1500A), and the outputs were recorded by an A/D converter (Digidata 1440A or Keithley 6514) connected to a computer. These electrical measurements were performed in ambient environments with ~40% relative humidity. The electrical recordings from the cardiac tissues were performed by applying a DC bias (5–10 mV) to one terminal of the graphene device with the other terminal grounded. The current was amplified with a home-built amplifier system and acquired at 20kHz by an A/D converter (Digidata 1440A, Molecular Devices) interfaced with computerized software (pClamp 10.7, Molecular Devices). Data analysis was carried out using OriginPro (version 2022, OriginLab).

Spiking energy calculation

The spiking energy is defined as the total energy consumption in the circuit during the spiking event, which is calculated by using the following equation:

$$E = \int_0^{t_p} V_i(I_R + I_c)dt = \int_0^{t_p} V_i\left(\frac{V_o}{R} + \frac{C \cdot dV_o}{dt}\right)dt$$

where V_i, t_p, and V_o are the input voltage, peak time, and the (instant) output voltage, respectively. The total circuit current consists of the components going through the resistor (I_R) and capacitor (I_C). Note that the energy consumption during the discharging process ($t_p \to \infty$) is the same as the pre-stored energy in the capacitor already included in the formula. This voltage-based calculation method is further verified by direct current and voltage measurements in the circuit (Supplementary Fig. 17).

Data availability

The data supporting the findings of this study are available within the article and its supplementary files. Source Data are provided with this paper. Any additional requests for information can be directed to, and will be fulfilled by, the corresponding author. Source data are provided with this paper.

References

1. Service, R. F. The Cyborg Era Begins. *Science* **340**, 1162–1165 (2013).
2. Chortos, A., Liu, J. & Bao, Z. A. Pursuing prosthetic electronic skin. *Nat. Mater.* **15**, 937–950 (2016).
3. Kim, D. H., Lu, N. S., Huang, Y. G. & Rogers, J. A. Materials for stretchable electronics in bioinspired and biointegrated devices. *MRS Bull.* **37**, 226–235 (2012).
4. Woods, G. A., Rommelfanger, N. J. & Hong, G. S. Bioinspired materials for bioelectronic neural interfaces. *Matter* **3**, 1087–1113 (2020).
5. Hong, G. S. & Lieber, C. M. Novel electrode technologies for neural recordings. *Nat. Rev. Neurosci.* **20**, 330–345 (2019).
6. Li, P., Kim, S. & Tian, B. Beyond 25 years of biomedical innovation in nano-bioelectronics. *Device* **2**, 100401 (2024).
7. Tang, X., He, Y. C. & Liu, J. Soft bioelectronics for cardiac interfaces. *Biophys. Rev.* **3**, 011301 (2022).
8. Jo, S. H. et al. Nanoscale memristor device as synapse in neuromorphic systems. *Nano Lett.* **10**, 1297–1301 (2010).
9. Prezioso, M. et al. Training and operation of an integrated neuromorphic network based on metal-oxide memristors. *Nature* **521**, 61–64 (2015).
10. Xia, Q. F. & Yang, J. J. Memristive crossbar arrays for brain-inspired computing. *Nat. Mater.* **18**, 309–323 (2019).
11. Zidan, M. A., Strachan, J. P. & Lu, W. D. The future of electronics based on memristive systems. *Nat. Electron* **1**, 22–29 (2018).
12. Choi, S., Yang, J. & Wang, G. Emerging memristive artificial synapses and neurons for energy-efficient neuromorphic computing. *Adv. Mater.* **32**, 2004659 (2020).
13. Tang, J. S. et al. Bridging biological and artificial neural networks with emerging neuromorphic devices: fundamentals, progress, and challenges. *Adv. Mater.* **31**, 1902761 (2019).
14. Fu, T. D., Fu, S. & Yao, J. Recent progress in bio-voltage memristors working with ultralow voltage of biological amplitude. *Nanoscale* **15**, 4669–4681 (2023).
15. Dai, S. L. et al. Intrinsically stretchable neuromorphic devices for on-body processing of health data with artificial intelligence. *Matter* **5**, 3375–3390 (2022).
16. Zhu, X. J., Wang, Q. W. & Lu, W. D. Memristor networks for real-time neural activity analysis. *Nat. Commun.* **11**, 2439 (2020).
17. Kim, Y. et al. A bioinspired flexible organic artificial afferent nerve. *Science* **360**, 998–1003 (2018).
18. Sarkar, T. et al. An organic artificial spiking neuron for in situ neuromorphic sensing and biointerfacing. *Nat. Electron* **5**, 774–783 (2022).
19. Cucchi, M. et al. Reservoir computing with biocompatible organic electrochemical networks for brain-inspired biosignal classification. *Sci. Adv.* **7**, eabh0693 (2021).
20. Zhang, X. M. et al. An Artificial Neuron Based on a Threshold Switching Memristor. *IEEE Electron Device Lett.* **39**, 308–311 (2018).
21. Wang, Z. R. et al. Fully memristive neural networks for pattern classification with unsupervised learning. *Nat. Electron* **1**, 137–145 (2018).
22. Pickett, M. D., Medeiros-Ribeiro, G. & Williams, R. S. A scalable neuristor built with Mott memristors. *Nat. Mater.* **12**, 114–117 (2013).
23. Wang, Z. R. et al. Capacitive neural network with neuro-transistors. *Nat. Commun.* **9**, 3208 (2018).
24. Harikesh, P. C. et al. Organic electrochemical neurons and synapses with ion mediated spiking. *Nat. Commun.* **13**, 901 (2022).
25. Fu, T. D. et al. Bioinspired bio-voltage memristors. *Nat. Commun.* **11**, 1861 (2020).

26. Harikesh, P. C. et al. Ion-tunable antiambipolarity in mixed ion-electron conducting polymers enables biorealistic organic electrochemical neurons. *Nat. Mater.* **22**, 242–248 (2023).
27. Chen, J. Q. et al. Reconfigurable Ag/HfO/NiO/Pt memristors with stable synchronous synaptic and neuronal functions for renewable homogeneous neuromorphic computing system. *Nano Lett.* **24**, 5371–5378 (2024).
28. Li, F. et al. An artificial visual neuron with multiplexed rate and time-to-first-spike coding. *Nat. Commun.* **15**, 3689 (2024).
29. Park, W. et al. High amplitude spike generator in Au nanodot-incorporated NbOx mott memristor. *Nano Lett.* **23**, 5399–5407 (2023).
30. Yuan, R. et al. A calibratable sensory neuron based on epitaxial VO for spike-based neuromorphic multisensory system. *Nat. Commun.* **13**, 3973 (2022).
31. Pei, Y. F. et al. Artificial visual perception nervous system based on low-dimensional material photoelectric memristors. *ACS Nano* **15**, 17319–17326 (2021).
32. Fu, T. D. et al. Self-sustained green neuromorphic interfaces. *Nat. Commun.* **12**, 3351 (2021).
33. Han, J. K. et al. Bioinspired photoresponsive single transistor neuron for a neuromorphic visual system. *Nano Lett.* **20**, 8781–8788 (2020).
34. Wu, Q. T. et al. Spike encoding with optic sensory neurons enable a pulse coupled neural network for ultraviolet image segmentation. *Nano Lett.* **20**, 8015–8023 (2020).
35. Wang, X. J. et al. Vertically integrated spiking cone photoreceptor arrays for color perception. *Nat. Commun.* **14**, 3444 (2023).
36. Bean, B. P. The action potential in mammalian central neurons. *Nat. Rev. Neurosci.* **8**, 451–465 (2007).
37. Ohno, T. et al. Short-term plasticity and long-term potentiation mimicked in single inorganic synapses. *Nat. Mater.* **10**, 591–595 (2011).
38. Hallermann, S., de Kock, C. P. J., Stuart, G. J. & Kole, M. H. P. State and location dependence of action potential metabolic cost in cortical pyramidal neurons. *Nat. Neurosci.* **15**, 1007–1014 (2012).
39. Lewis, J. E., Gilmour, K. M., Moorhead, M. J., Perry, S. F. & Markham, M. R. Action Potential Energetics at the Organismal Level Reveal a Trade-Off in Efficiency at High Firing Rates. *J. Neurosci.* **34**, 197–201 (2014).
40. Wang, S. S. H. et al. Functional trade-offs in white matter axonal scaling. *J. Neurosci.* **28**, 4047–4056 (2008).
41. Wang, Z. R. et al. Threshold switching of Ag or Cu in dielectrics: materials, mechanism, and applications. *Adv. Funct. Mater.* **28**, 1704862 (2018).
42. Lovley, D. R. & Yao, J. Intrinsically conductive microbial nanowires for 'green' electronics with novel functions. *Trends Biotechnol.* **39**, 940–952 (2021).
43. Liu, X. M. et al. Power generation from ambient humidity using protein nanowires. *Nature* **578**, 550–554 (2020).
44. Liu, X. M., Gao, H. Y., Sun, L. & Yao, J. Generic air-gen effect in nanoporous materials for sustainable energy harvesting from air humidity. *Adv. Mater.* **36**, 2300748 (2024).
45. Zipser, B. Voltage-modulated membrane resistance in coupled leech neurons. *J. Neurophysiol.* **42**, 465–475 (1979).
46. Kawaguchi, Y. Distinct firing patterns of neuronal subtypes in cortical synchronized activities. *J. Neurosci.* **21**, 7261–7272 (2001).
47. Golowasch, J. et al. Membrane capacitance measurements revisited: dependence of capacitance value on measurement method in nonisopotential neurons. *J. Neurophysiol.* **102**, 2161–2175 (2009).
48. Chen, L. B. et al. Conditional knockout of $Na_V1.6$ in adult mice ameliorates neuropathic pain. *Sci. Rep.* **8**, 3845 (2018).
49. Zhao, H. et al. Upregulation of Beta4 subunit of BK(Ca) channels in the anterior cingulate cortex contributes to mechanical allodynia associated anxiety-like behaviors. *Mol. Brain* **13**, 22 (2020).
50. Reijntjes, D. O. J. et al. Sodium-activated potassium channels shape peripheral auditory function and activity of the primary auditory neurons in mice. *Sci. Rep.* **9**, 2573 (2019).
51. Gaba, S., Sheridan, P., Zhou, J. T., Choi, S. & Lu, W. Stochastic memristive devices for computing and neuromorphic applications. *Nanoscale* **5**, 5872–5878 (2013).
52. Holt, G. R., Softky, W. R., Koch, C. & Douglas, R. J. Comparison of discharge variability in vitro and in vivo in cat visual cortex neurons. *J. Neurophysiol.* **75**, 1806–1814 (1996).
53. Magee, J. C. Dendritic integration of excitatory synaptic input. *Nat. Rev. Neurosci.* **1**, 181–190 (2000).
54. Magee, J. C. Dendritic normalizes temporal summation in hippocampal CA1 neurons. *Nat. Neurosci.* **2**, U9–U9 (1999).
55. Wang, B. et al. Firing frequency maxima of fast-spiking neurons in human, monkey, and mouse neocortex. *Front. Cell Neurosci.* **10**, 239 (2016).
56. Tewari, B. P. et al. Perineuronal nets decrease membrane capacitance of peritumoral fast spiking interneurons in a model of epilepsy. *Nat. Commun.* **9**, 4724 (2018).
57. Rong, Z. X., Bhatnagar, P., Yang, J. J. & Chen, Y. Capacitor-free scalable CMOS neuron circuit with compact design and low power consumption. *IEEE Access* **12**, 158258–158265 (2024).
58. Sourikopoulos, I. et al. A 4-fJ/spike artificial neuron in 65 nm CMOS technology. *Front. Neurosci.* **11**, 123 (2017).
59. Khanday, M. A., Khanday, F. A. & Bashir, F. Single SiGe transistor based energy-efficient leaky integrate-and-fire neuron for neuromorphic computing. *Neural Process Lett.* **55**, 6997–7007 (2023).
60. Ren, H. H. et al. An ion-mediated spiking chemical neuron based on mott memristor. *Adv. Mater.* **36**, 2403678 (2024).
61. Sheffler, Z. M., Reddy, V. & Pillarisetty, L. S. Physiology, Neurotransmitters. In: *StatPearls* (StatPearls Publishing, 2023).
62. Levitan, I. B. Modulation of ion channels in neurons and other cells. *Annu. Rev. Neurosci.* **11**, 119–136 (1988).
63. Hodgkin, A. L. & Katz, B. The effect of sodium ions on the electrical activity of the giant axon of the squid. *J. Physiol.* **108**, 37–77 (1949).
64. Wang, Z. R., Hesketh, J. C. & Fedida, D. A high-Na conduction state during recovery from inactivation in the K channel Kv1.5. *Biophys. J.* **79**, 2416–2433 (2000).
65. Demuru, S., Kunnel, B. P. & Briand, D. Real-time multi-ion detection in the sweat concentration range enabled by flexible, printed, and microfluidics-integrated organic transistor arrays. *Adv. Mater. Technol.* **5**, 2000328 (2020).
66. Arakaki, X. et al. Extracellular sodium modulates the excitability of cultured hippocampal pyramidal cells. *Brain Res* **1401**, 85–94 (2011).
67. Nicola, S. M., Surmeier, D. T. & Malenka, R. C. Dopaminergic modulation of neuronal excitability in the striatum and nucleus accumbens. *Annu. Rev. Neurosci.* **23**, 185–215 (2000).
68. Akaike, A., Ohno, Y., Sasa, M. & Takaori, S. Excitatory and inhibitory effects of dopamine on neuronal activity of the caudate nucleus neurons in vitro. *Brain Res.* **418**, 262–272 (1987).
69. Zhang, M. et al. High-performance dopamine sensors based on whole graphene solution- gated transistors. *Adv. Funct. Mater.* **24**, 978–985 (2014).
70. Moore, A. R., Zhou, W. L., Potapenko, E. S., Kim, E. J. & Antic, S. D. Brief dopaminergic stimulations produce transient physiological changes in prefrontal pyramidal neurons. *Brain Res.* **1370**, 1–15 (2011).
71. Wise, R. A. Dopamine, learning and motivation. *Nat. Rev. Neurosci.* **5**, 483–494 (2004).
72. Cui, Y., Wei, Q. Q., Park, H. K. & Lieber, C. M. Nanowire nanosensors for highly sensitive and selective detection of biological and chemical species. *Science* **293**, 1289–1292 (2001).

73. Li, Y. X. et al. Recent advances in molecularly imprinted polymer-based electrochemical sensors. *Biosens. Bioelectron.* **249**, 116018 (2024).
74. Lekbach, Y. et al. Microbial nanowires with genetically modified peptide ligands to sustainably fabricate electronic sensing devices. *Biosens. Bioelectron.* **226**, 115147 (2023).
75. Sonawane, J. M. et al. Sensing devices fabricated with expressing genetically tunable nanowires incorporated into a water-stable polymer. *Biosens. Bioelectron.* **278**, 117378 (2025).
76. Sun, H. D. et al. Complementary logic circuits based on high-performance n-type organic electrochemical transistors. *Adv. Mater.* **30**, 1704916 (2018).
77. Laswick, Z. et al. Tunable anti-ambipolar vertical bilayer organic electrochemical transistor enable neuromorphic retinal pathway. *Nat. Commun.* **15**, 6309 (2024).
78. Li, Q. et al. Cyborg organoids: implantation of nanoelectronics via organogenesis for tissue-wide electrophysiology. *Nano Lett.* **19**, 5781–5789 (2019).
79. Gao, H. Y. et al. Graphene-integrated mesh electronics with converged multifunctionality for tracking multimodal excitation-contraction dynamics in cardiac microtissues. *Nat. Commun.* **15**, 2321 (2024).
80. Gao, H. Y. et al. Bioinspired two-in-one nanotransistor sensor for the simultaneous measurements of electrical and mechanical cellular responses. *Sci. Adv.* **8**, eabn2485 (2022).
81. Rusakov, D. A., Savtchenko, L. P., Zheng, K. Y. & Henley, J. M. Shaping the synaptic signal: molecular mobility inside and outside the cleft. *Trends Neurosci.* **34**, 359–369 (2011).
82. Farronato, M. et al. Seizure detection via reservoir computing in MoS_2-based charge trap memory devices. *Sci. Adv.* **11**, eadr3241 (2025).
83. Sbandati, C. et al. Single-trial detection of auditory cues from the rat brain using memristors. *Sci. Adv.* **10**, eadp7613 (2024).
84. Wang, H. Z. et al. Low-temperature copper bonding strategy with graphene interlayer. *ACS Nano* **12**, 2395–2402 (2018).

Acknowledgements

J.Y. acknowledges support from the Army Research Office W911NF2210027. J.Y. and D.R.L. acknowledge support from National Science Foundation (NSF) DMR-2027102. J.Y. also acknowledges supports from National Institutes of Health (NIH) R21EB030216, R33HL175683, NSF CCSS-2345733, and Alfred P. Sloan Foundation (FG-2022-18452). Z.W. and J.K. acknowledge support from the Semiconductor Research Corporation Center 7 in JUMP 2.0 (award no. 145105-21913). Part of the device fabrication work was conducted in the clean room of the Center for Hierarchical Manufacturing (CHM), an NSF Nanoscale Science and Engineering Center (NSEC) located at the University of Massachusetts, Amherst.

Author contributions

S.F. and J.Y. conceived the project and designed experiments. S.F. performed experiments in device fabrication, characterization, circuit design, and electrical measurements. H.G. and X.W. helped with the fabrication of mesh devices, cell culture, imaging, and in vitro electrical recordings. S.W. helped with the fabricaiton of PEDOT:PSS sensors. T.W. performed protein nanowire preparation and imaging. D.R.L. oversaw protein nanowire production. E.Z. and J.K. helped with graphene synthesis. J.Y. and S.F. wrote the paper. All authors discussed the results and implications and commented on the manuscript.

Competing interests

The authors declare no competing interests.

Additional information

Supplementary information The online version contains supplementary material available at https://doi.org/10.1038/s41467-025-63640-7.

Correspondence and requests for materials should be addressed to Jun Yao.

Peer review information *Nature Communications* thanks Ugo Bruno, and the other, anonymous, reviewer(s) for their contribution to the peer review of this work. A peer review file is available.